IEEE Access
Multidisciplinary | Rapid Review | Open Access Journal

Date of publication xxxx 00, 0000, date of current version xxxx 00, 0000.

Digital Object Identifier 10.1109/ACCESS.2017.Doi Number

A Stepwise Optimal Design Applied to an Interior Permanent Magnet Synchronous Motor for Electric Vehicle Traction Applications

Jae-Gil Lee[1] and Dong-Kuk Lim[2], (Member, IEEE)

[1]Intelligent Mechatronics Research Center, Korea Electronics Technology Institute, Bucheon 14502, South Korea
[2]School of Electrical Engineering, University of Ulsan, Ulsan 44610, South Korea

Corresponding author: Dong-Kuk Lim (e-mail: ldk8745@ulsan.ac.kr)

This work was supported by the National Research Foundation of Korea (NRF) funded by the Korean Government (Ministry of Science and ICT) under Grant 2019R1F1A1061132.

ABSTRACT This paper presents a stepwise optimal design (SOD) for an interior permanent magnet synchronous motor (IPMSM) applied to electric vehicle traction, which sequentially utilizes a magnetic equivalent circuit (MEC), finite element analysis (FEA), and a newly proposed optimization algorithm. The design of an IPMSM for the traction motor of a fuel cell electric vehicle (FCEV) is challenging due to its tough requirements, such as high torque density, high efficiency, and low torque ripple; as a result, an iterative trial and error process is required. However, FEA, which is the most generally used analysis technique for electric machine design, has a drawback in terms of the analysis time required when being applied to the entire design process. In this regard, the proposed SOD is presented, which consists of initial, detailed, and optimal design stages, to design an IPMSM with a reasonable design time.

INDEX TERMS Fuel cell electric vehicle, interior permanent magnet motor, magnetic equivalent circuit, optimal design

I. INTRODUCTION

An important part of the movement toward a more eco-friendly automobile industry, fuel cell electric vehicles (FCEVs) powered by hydrogen are emerging as the next generation of automobiles in the near future [1]-[3]. The traction motor of the FCEV requires a wide speed range and compactness due to the limited mounting space; thus, high-efficiency and high-torque-density characteristics are required [4], [5]. An interior permanent magnet synchronous motor (IPMSM) is the most suitable type for FCEV traction applications in terms of the high-torque and high-efficiency performances covering a wide speed range because the excellent field-weakening characteristics, reluctance torque, and magnet torque can be utilized [6]-[9].

In the design of an IPMSM, finite element analysis (FEA), which can analyze complex structures and nonlinear characteristics, is commonly used because accurate electromagnetic field analysis is essential for accurate estimation of motor performances. However, since the design of the IPMSM requires a considerable amount of analysis, it is time-consuming for the designer to utilize FEA for the whole design procedure [10]-[12].

Meanwhile, a magnetic equivalent circuit (MEC) can be used to rapidly analyze the characteristics of various types of electric motors, such as surface-mounted permanent magnet (SPM) motors [13]-[16]; spoke-type motors [17], [18]; brushless DC (BLDC) motors [19], [20]; interior-mounted permanent magnet (IPM) motors [21]-[24]; and induction motors [25], [26]. Although the MEC technique has the advantage of a short computation time, it also has difficulties directly utilizing the whole design procedure due to its somewhat lower accuracy compared to the FEA.

To address this problem, this study presents a stepwise optimal design (SOD), which performs the design process step by step. At first, in the initial design stage, the sequential stage MEC (which can be utilized even for a multi-layered IPMSM while considering the saturation effect) is used to quickly derive motor performances, including the back-electromotive force (back-EMF), total harmonic distortion (THD), average torque, and terminal voltage, according to the design variables of the motor [24]. In the second stage, the electromagnetic characteristics that are difficult to calculate by the MEC, such as the cogging

This article has been accepted for publication in a future issue of this journal, but has not been fully edited. Content may change prior to final publication. Citation information: DOI 10.1109/ACCESS.2021.3105119, IEEE Access

torque, torque ripple, demagnetization aspect of a permanent magnet (PM), and mechanical stress, are analyzed using FEA during the detailed design stage. In this stage, the thermal characteristics are also analyzed by utilizing lumped parameter thermal network (LPTN) analysis. Finally, optimal design using an initial model obtained from the previous design stages is used to improve the machine performance and to derive the optimal design with the design variables and objectives. In previous study, *Yoo et al.* presented a multimodal optimization algorithm which is the big-bang big-crunch multimodal optimization algorithm: BB-MOA) based on the surrogate model [27]. They reported the BB-MOA reduced the number of function evaluations by about 90% compared to the probabilistic optimization algorithms. In this study, a simpler and improved algorithm based on the Kriging surrogate model is developed to minimize the computational cost for the optimization time.

The remaining parts of this paper are organized as follows. The main requirements and parameters for the design of the FCEV traction motor are presented in Section II. Sections III, IV, and V describe the initial design by MEC, detailed design by FEA, and optimal design by the optimization algorithm, respectively. Finally, Section VI concludes this paper.

II. Stepwise optimal design of the IPMSM for an FCEV

A. Design requirements

This paper describes an SOD based on an IPMSM design for FCEV traction applications. The specifications and requirements of the IPMSM are shown in Table I.

At first, the dimensions of the stator outer diameter and axial length were determined as 240 mm and 230 mm, respectively, which are limited in size due to the mounting space. The number of poles should be determined by considering the maximum frequency of switching components in the inverter depending on the driving speed. In this design, the number of poles was determined as eight, which is the highest possible number that guarantees the frequency capacity.

TABLE I
DESIGN REQUIREMENTS

Items	unit	Values
Number of poles/slots/phases	EA	8/36/3
Max. torque	Nm	300
Max. power	kW	100
Stator outer diameter	mm	240
Stator inner diameter	mm	172
Air-gap length	mm	1
Stack length	mm	230
Required maximal torque	Nm	310
Remanence of PM	T	1.3
Thickness of steel sheet	mm	0.35
Maximal current	A	520
DC link voltage	V	240

Next, the number of slots was chosen as 36 by considering several aspects, e.g., the number of available parallel circuits, the winding factor, the period of the cogging torque, and the manufacturability.

Meanwhile, various rotor topologies according to the PM construction inside the rotor core, such as V-shape, double V-shape, or delta shape, can be applied to the IPMSM [28]-[31]. In this research, a multi-segmented and multi-layered (MSML) structure is selected owing to advantages like a high degree of design freedom, convenience of manufacturing, and good space utilization with excellent electromagnetic performances, e.g., high reluctance torque, low torque ripple, and good flux-weakening properties.

The required maximal torque value is 300 Nm and the maximal power value is 100 kW from 3,600 r/min to 9,000 r/min in the flux-weakening operating region. The instantaneous current limitation and DC link voltage are determined as specifications of the mounted components of the inverter drive. Meanwhile, the steel sheet thickness and PM remanence are chosen as 0.35 mm and 1.3 T, respectively, by considering the high-torque-density and the high-efficiency design. The corresponding requirements described above are listed in Table I.

B. Overview of the SOD of the IPMSM

This paper describes the SOD procedure, which is divided into three design stages by sequentially utilizing different analysis methods and design strategies. Fig. 1 shows the whole procedure of the proposed SOD, which consists of an initial design stage using an MEC, a detailed design stage using FEA, and an optimal design stage using an optimization algorithm. Detailed descriptions of each design stage are given in the next sections.

III. Initial design using a MEC model

In the initial stage of the motor design, it is very important to rapidly grasp how the motor performances vary with a variety of design parameters, including the machine dimensions, materials, and input conditions. The MEC concept, which simplifies the complex motor structure into lumped circuit parameters, can be effectively utilized in the initial design stage due to its great merit in terms of the computational time compared to the commonly used analysis technique, i.e., FEA, even if there are some inevitable calculation errors.

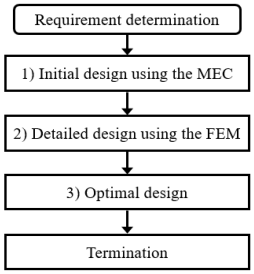

FIGURE 1. Overview of the whole procedure for the proposed SOD.

This article has been accepted for publication in a future issue of this journal, but has not been fully edited. Content may change prior to final publication. Citation information: DOI 10.1109/ACCESS.2021.3105119, IEEE Access

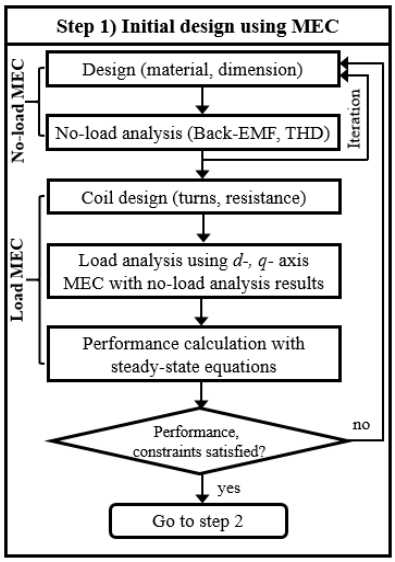

FIGURE 2. **Flowchart of the initial design stage.**

For example, the analysis time taken to estimate the average torque for each current phase angle of a motor model can be significantly reduced from several hours to a few seconds. The total design process can become more efficient if as many as possible parameters are considered in the initial design stage. The saved design time can be utilized later to improve the design quality by considering optimization, multi-physics, and systematic matters.

Fig. 2 shows the flowchart of the initial design stage, which consists of no-load and load MECs. At first, the outer diameter and height of the motor in the limited space are determined. The material of the iron core and permanent magnet are also considered in terms of the cost and required operating point. When designing the example EV traction motor in this study, an electrical steel sheet with excellent iron loss characteristics in the high-speed range is preferred. Meanwhile, the EV motor should maintain robust performance, even at high-temperature conditions. Hence, an NdFeB-series rare earth PM that has high coercivity and excellent tolerance for demagnetization is preferred. Using the determined material and required size, no-load analysis is performed according to the shape of the motor determined from various design variables.

A. No-load MEC analysis

First, referring to previous studies [3], [4], the MSML IPMSM with the design parameters shown in Fig. 3 is modeled as an MEC model for the no-load analysis. The no-load MEC model consists of flux source, magnet reluctance, air-gap reluctance, bridge leakage, and center post leakage components, as shown in Fig. 4. Here, we use a symmetrical circuit and assume infinite permeability for the iron core for simplification. In Fig. 4, the flux components (ϕ_{rij}: the flux sources over the jth PM in ith layer, ϕ_{i}: the leakage flux around the PM in ith layer, ϕ_{mbi}: the leakage flux of bridge area in ith layer, ϕ_{mci}: the leakage flux of center-post in

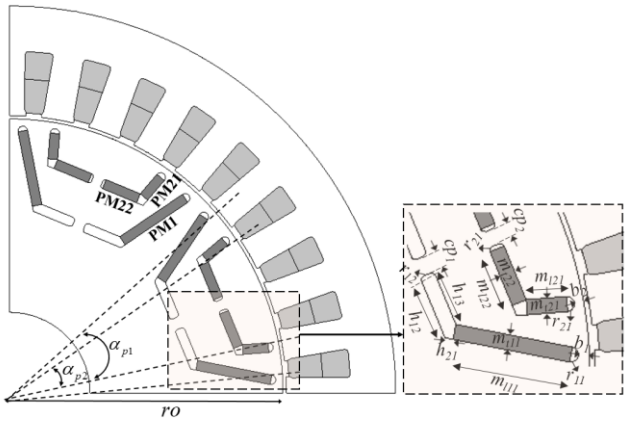

FIGURE 3. **Design parameters of the IPMSM for the FCEV.**

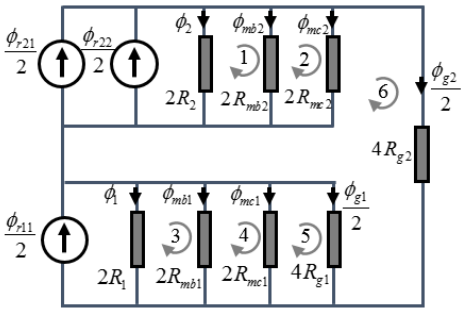

FIGURE 4. **The simplified MEC for the no-load analysis of the IPMSM.**

ith layer, and ϕ_{gi}: the flux passing the air-gap area) can respectively be calculated by (1)-(3) with dimension parameters represented in Fig. 4.

$$\phi_{rij} = B_r A_{mij} \tag{1}$$

$$\phi_{mbi} = B_{sat} A_{mbi} = B_{sat} b_i L_{st} \tag{2}$$

$$\phi_{mci} = B_{sat} A_{mci} = B_{sat} cp_i L_{st} . \tag{3}$$

Moreover, the reluctance components (R_{gi}: the air-gap reluctances of ith pole layer and R_i:the total leakage reluctance of ith pole layer) be calculated by (4)-(8) , where g, μ_0, α_{pi}, so, Np, and L_{st} represent the air-gap length, permeability of air, pole-arc-to-pole pitch ratio of ith pole layer, length of slot opening, number of poles, and stacking length respectively. Meanwhile, the leakage reluctances R_{moij} and R_{mlij}, which compose of R_i represent the self-leakage and the end-leakage of jth PM in ith pole layer. More details calculate the circuit parameters can be found in [23]-[24].

$$R_{gi} = g / \mu_0 A_{gi} \tag{4}$$

$$A_{g1} = (\alpha_{p1} - \alpha_{p2}) \frac{2\pi(so + g/2)L_{st}}{N_p} \tag{5}$$

$$A_{g2} = \alpha_{p2} \frac{2\pi(so + g/2)L_{st}}{N_p} \tag{6}$$

$$R_1 = 2R_{mo11} // R_{ml11} // R_{ml12} \tag{7}$$

$$R_2 = 2R_{mo21} // R_{ml21} // R_{ml22} // 2R_{ml22} // R_{ml23} // R_{ml24} . \tag{8}$$

This article has been accepted for publication in a future issue of this journal, but has not been fully edited. Content may change prior to final publication. Citation information: DOI 10.1109/ACCESS.2021.3105119, IEEE Access

Then, The MEC model in Fig. 4 can be represented as (9) by using Kirchhoff's rules, where the air-gap flux values ϕ_{g1} and ϕ_{g2} can be solved by calculating the inverse matrix, and the corresponding air-gap flux densities B_{g1} and B_{g2} are obtained. Finally, the air-gap flux density considering the slotting effects can be derived by applying the conformal mapping technique, which analytically calculates the permeance function of the stator slot, to the previously calculated air-gap flux densities [32]-[33].

$$\begin{pmatrix} R_1 & 0 & -R_{g1} & 0 \\ 0 & R_2 & R_{g1} & -R_{g2} \\ 0 & 2 & 0 & 1 \\ 2 & -2 & 1 & 0 \end{pmatrix} \begin{pmatrix} \phi_1 \\ \phi_2 \\ \phi_3 \\ \phi_4 \end{pmatrix} = \begin{pmatrix} 0 \\ 0 \\ \phi_{r21} + \phi_{r22} - 2\phi_{mb2} - 2\phi_{mc2} \\ \phi_{r11} + \phi_{mb2} - 2\phi_{mc2} - \phi_{r21} - \phi_{r22} - 2\phi_{mb1} - 2\phi_{mc1} \end{pmatrix} \quad (9)$$

Then, the back-EMF can be calculated by (10) after deriving the flux linkage by summing up the air-gap flux density according to the winding pattern.

In (10), e_a, λ_a, θ, and ω_r represent the back-EMF, flux linkage of phase *A*, angular position, and rotational speed of the rotor, respectively.

$$e_A = \frac{d\lambda_A}{dt} = \frac{d\theta}{dt}\frac{d\lambda_A}{dt} = \omega_r \frac{\Delta\lambda_A}{\Delta\theta} \quad (10)$$

Fig. 5 shows comparison result of the back-EMF for the verification of no-load MEC with FEA. It can be seen that the results from the MEC and FEA are well matched in a small difference. In the no-design process, many candidate designs with varying the design variables, e.g., the pole arc ratio, magnet usage and dimension, center post, bridge, and flux barrier (shown in Fig. 3) can be analyzed. Here, the total harmonic distortion (THD), which can be calculated by (11), must be suppressed due to the effects not only on the torque fluctuation appearing with multiplied by the current harmonics but the controllability as well. In (11), the subscript *i* represents the harmonic index. Fig. 6 illustrates the THD characteristics of the back-EMF according to α_{p1} and α_{p2}, which represent the pole arc to pole pitch ratio of each magnet layer of the IPMSM for the FCEV.

$$THD = \frac{\sqrt{e_2^2 + e_3^2 + e_4^2 + \cdots}}{e_1} \times 100 \quad (11)$$

B. On-load MEC analysis

Before analyzing the on-load performance of the motor, the coil must be specified by considering the back-EMF constant, maximum current, winding connection, continuous current density, slot dimension, and coil fill factor. Then, the number of coils and coil diameter determine the armature resistance. Meanwhile, the on-load analysis of the synchronous motor can be conducted by dividing it into *d*-axis and *q*-axis circuit analyses in the coordinate system while rotating at the synchronous speed [34]-[36].

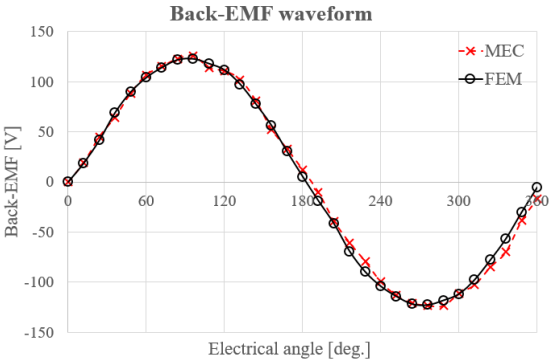

FIGURE 5. Back-EMF waveform comparison calculated by the MEC and FEA.

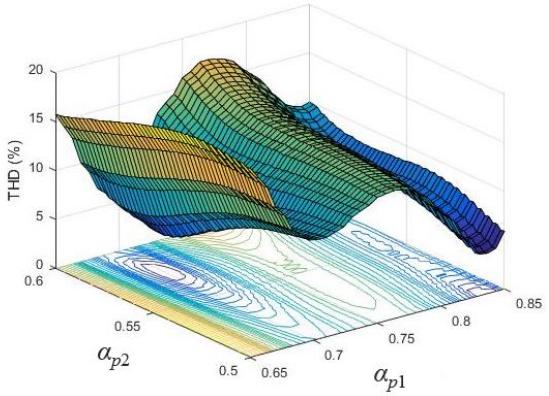

FIGURE 6. Illustration of the THD analysis results with varying pole arc to pole pitch ratios with the no-load MEC model

In the *q*-axis circuit, the flux made by the armature current with a phase angle 90° ahead of the N pole of the rotor is applied. At this time, the magnetic flux caused by the current forms a flux path through the iron core, mainly bypassing the PMs, which are magnetically regarded as air. Thus, the saturation degree of the iron core is quite high. On the other hand, the *d*-axis armature current with a phase angle of 0° forms the flux path through the PMs, so that the permeability of the iron core can be regarded as infinity. Fig. 7 shows the on-load MEC models of the IPMSM for the FCEV, in which the reluctance elements are constructed to reflect the permeability. In each MEC model, the air-gap flux density is calculated in a similar manner to the no-load MEC procedure, and then the flux linkage values λ_d and λ_q can be derived [24].

Finally, the average torque and induced voltage can be calculated by characteristic equations (12) -(15).

$$T_{avg} = \frac{3}{2}\frac{N_p}{2}(\lambda_d i_q - \lambda_q i_d) \quad (12)$$

$$V_d = R_s i_d - \omega_r \lambda_q \quad (13)$$

$$V_q = R_s i_q + \omega_r \lambda_d \quad (14)$$

$$V_r = \sqrt{V_d^2 + V_q^2} \quad (15)$$

This article has been accepted for publication in a future issue of this journal, but has not been fully edited. Content may change prior to final publication. Citation information: DOI 10.1109/ACCESS.2021.3105119, IEEE Access

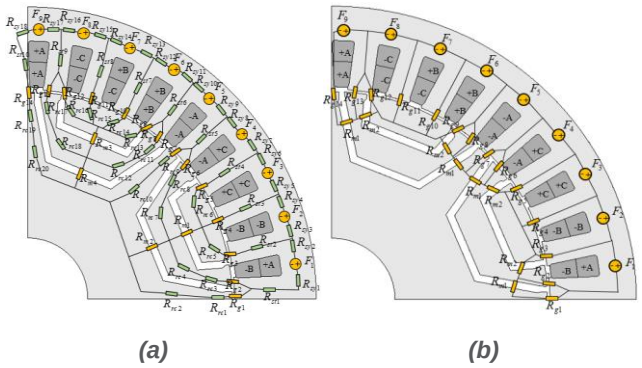

FIGURE 7. **The on-load MEC model of the IPMSM: (a) *q*-axis model and (b) *d*-axis model.**

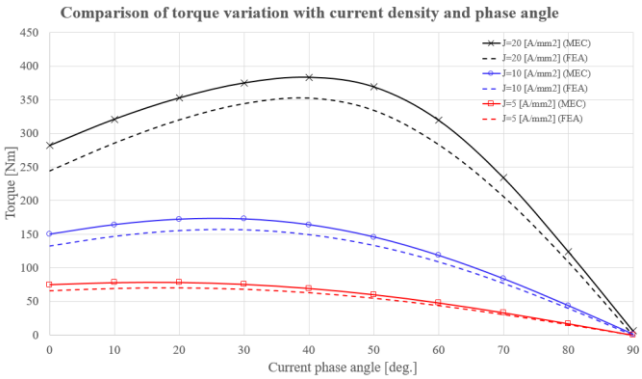

FIGURE 8. **Comparison of average torque variation with the current phase angle according to the current density calculated by the MEC and the FEA.**

In this step, the iterative design modification and analyses used to obtain design candidates that satisfy the constraints and requirements are conducted. When the iteration is terminated, a few candidates can be obtained and the designer can choose one or more of them to proceed to the next design step.

For the IPMSM analysis, the maximum torque per ampere (MTPA) point should be analyzed for each amplitude and current phase angle whenever the iterative design is proceeded, which is very time-consuming. However, the MEC model completes this process in just a few seconds, so there is no time burden, even for designs with many iterations. In Fig.8, the average torque variation according to the current densities and phase angles for the verification of on-load characteristic is presented. Even though there is some difference between the results of MEC and FEA, the analysis time can be significantly shortened by using MEC. In terms of time consumption, it was possible to analysis each design case in less than 3 seconds by using MEC analysis with AMD Ryzen 7 3700X 8-core/ 3.59GHZ CPU and 16 GB RAM. While, the FEA required about 2 minutes to analyze a design case in the same computational environment. Overall, it is concluded that the analysis time can be reduced by 97% by introducing the MEC.

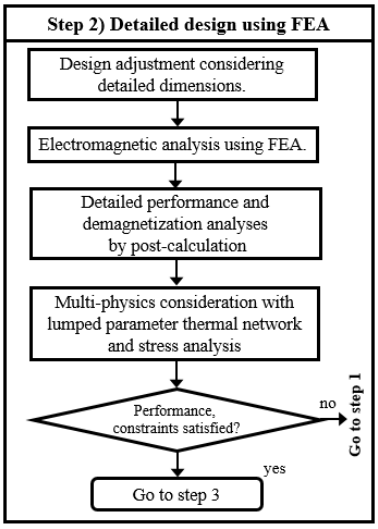

FIGURE 9. **Flowchart of the detailed design stage.**

IV. Detailed design using FEA

In the detailed design stage, FEA is used to analyze various characteristics with detailed considerations. The FEA can be utilized to accurately analyze electromagnetic nonlinear characteristics of local parts and multi-physical phenomena, such as mechanical stress. In Section III, the MEC analysis was used to calculate the flux distribution by a few number of lumped parameters simplifying the motor model. In detail, some geometries (i.e. pole shoe fillet or rounding of teeth, rounding on the slot back yoke side) which have little influence on the overall field distribution, were ignored in the MEC model for the simplification. However, they can affect the local filed distribution and machine performances. Hence, the fine adjustment for reflecting such detailed shapes are conducted before FEM analysis.

The detailed design concept is represented in Fig. 9. Here, the complicated and nonlinear characteristics in the local area, are analyzed via FEA. In addition, the detailed electromagnetic field distribution is analyzed to simulate the transient performances. Then, the post-calculation is conducted to estimate various aspects, including demagnetization of the PMs; this is especially important in the high-temperature environment for EV applications. Also, the stress analysis is conducted; this simulates the durability of the iron core by the centrifugal force in high-speed.

A. Detailed electromagnetic analyses

In the initial design stage, MEC was used to model the shape of the motor by using rough parameters, and only some of the steady-state characteristics were analyzed. On the other hand, in the detailed design stage, the performance characteristics, e.g., the cogging torque, torque ripple, iron loss, and efficiency considering the detailed shape and rotor position with the rotational angle, are analyzed through FEA. Here, torque-speed curve and efficiency maps over the entire driving range can also be calculated. Then, iterative design

This article has been accepted for publication in a future issue of this journal, but has not been fully edited. Content may change prior to final publication. Citation information: DOI 10.1109/ACCESS.2021.3105119, IEEE Access

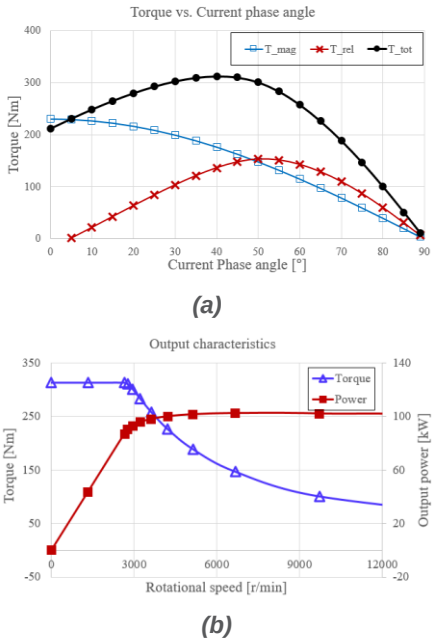

FIGURE 10. Output characteristics calculated by FEA:

(a) Analysis points of PMs and (b) analysis results.

and analyses are performed until a solution that meets the requirements is obtained. Fig. 10 shows the output characteristics calculated by FEA for the example IPMSM for EV traction in this study. At this stage, the design plan for the improvement is determined by analyzing the output characteristics by dividing the torque into magnet and reluctance torque and the output characteristic with and efficiency for each operating point and the operating range with flux weakening control. In addition, in order to improve characteristics like the cogging torque and torque ripple, which cause vibration and noise in the vehicle drive system, the magnetic flux path is smoothly improved by modifying the detailed shape in the vicinity of the gaps of the stator and the rotor.

B. Lumped parameter thermal analysis

During motor design, thermal analysis must be performed to prevent extreme situations, such as insulation breakdown of coils and permanent performance distortion due to irreversible thermal demagnetization of permanent magnets. Thermal analysis of electric motors can be mainly performed using computational fluid dynamics (CFD) [37]-[39] and a lumped parameter thermal network (LPTN) [39]-[41]. Specifically, it is effective to use a LPTN, which has the advantages of a short analysis time and convenience of modeling in the design stage. In this study, thermal analysis at continuous rating of a water-cooled EV driving system was performed using an LPTN. Fig. 11 (a) shows a simplified LPTN and (b) shows the analysis results of the thermal characteristics according to the driving time in the main parts of the motor: i.e., the PM, winding, and housing.

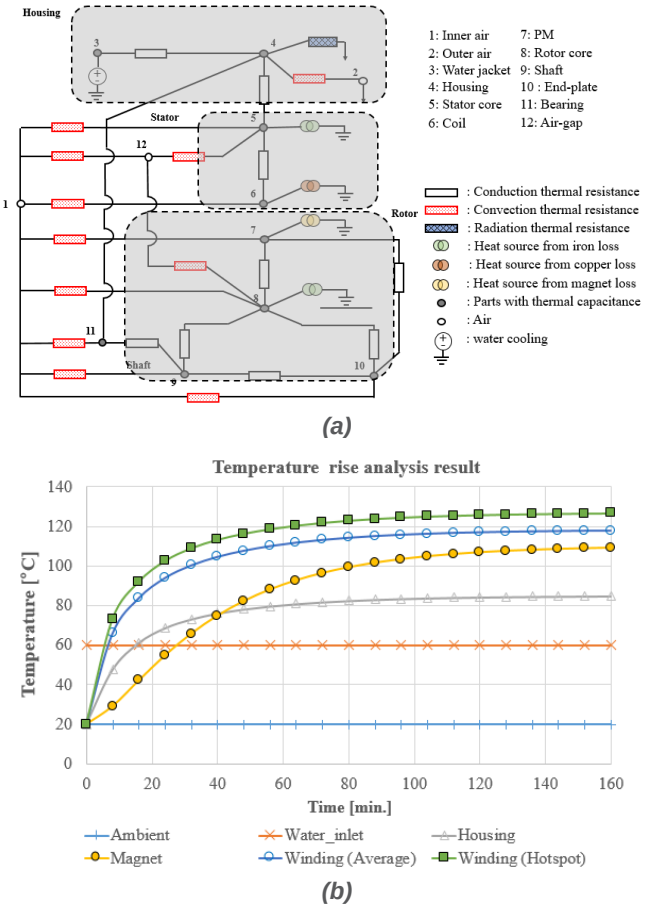

FIGURE 11. Thermal analysis using the LPTN:

(a) Developed LPTN and (b) analysis results.

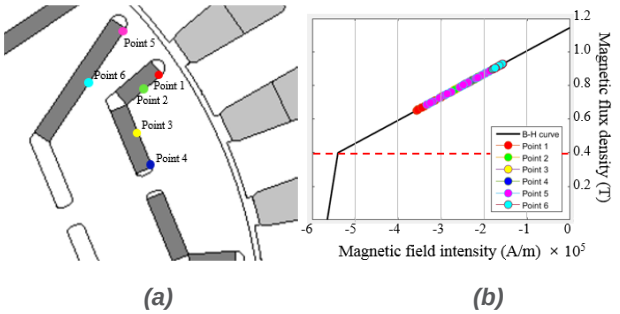

FIGURE 12. Demagnetization analysis of the IPMSM for the FCEV: (a) Analysis points of PMs and (b) analysis results.

C. Demagnetization analysis

Demagnetization analysis of PMs and stress analysis at high speeds is necessary in the IPMSM. Traction motors generally operate at a high current density due to their compact size, resulting in high-temperature driving conditions. Even though the NdFeB series PM has a superior heat tolerance, the remanence decreases at higher temperatures with a temperature constant κ according to (16). Here, Br, the subscript 0, and T represent the remanence of PM, the initial value, and the temperature, respectively. In particular, a high *d*-axis armature current is applied for flux-weakening control

This article has been accepted for publication in a future issue of this journal, but has not been fully edited. Content may change prior to final publication. Citation information: DOI 10.1109/ACCESS.2021.3105119, IEEE Access

due to the DC link voltage limit during high-speed operation. In this situation, irreversible magnetization can occur if the local operating point of the PM falls below the knee point of the B-H curve. Fig. 12 shows the demagnetization analysis results on a few points of the PM when the highest demagnetizing field of the instantaneous current with a 90° phase angle is induced; this is the toughest condition.

$$B_r = B_{r0}(1+\kappa\frac{T-T_0}{100}) \quad (16)$$

Fig. 12 (b) can be derived by using (17)-(18) based on the electromagnetic field analysis values B_i and H_i for an electrical period of the element *i*, where the subscripts *x* and *y* represent the projection values on the *x*-axis and *y*-axis, respectively, and α is the magnetization angle. As a result, it can be confirmed that even the edges of PMs, which are largely influenced by the demagnetizing field, operate above the knee point.

$$B_i = B_{ix}\cos\alpha + B_{iy}\sin\alpha \quad (17)$$

$$H_i = H_{ix}\cos\alpha + H_{iy}\sin\alpha \quad (18)$$

D. Stress analysis

For the high-speed operation of the IPMSM, the stress analysis of the rotor iron core (especially the stress on the bridges and center posts caused by the centrifugal force of the PM) must be considered to prevent structural breakage. It is essential to analyze the stress caused by the centrifugal force of the rotor during high-speed rotation of the IPM motor. In general, it is advantageous to reduce the thickness of the center post and the bridge of the rotor to minimize the leakage magnetic flux. However, the mechanical stress strength in the local area of the laminated steel varies with the rotor structure, which requires additional analysis. Hence, the verification of the mechanical stress as well as the electromagnetic performance via FEA should be included in the design process.

In addition, Fig. 13 shows the stress analysis using the structural FEA results at 10,000 r/min, which is higher than the required maximum speed of the target machine. In the analysis results, the point with the highest stress is near the center post (278 MPa).

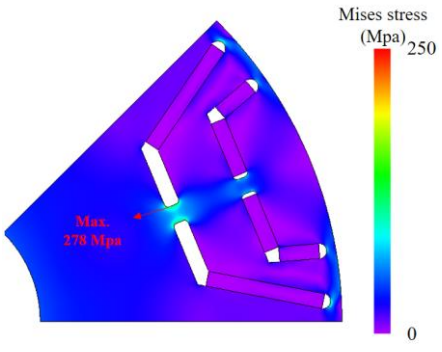

FIGURE 13. Von misses stress distribution of the IPMSM.

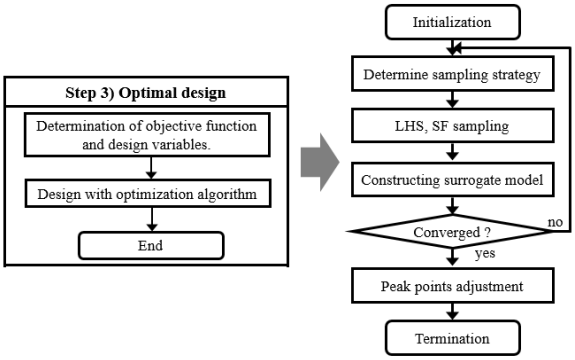

FIGURE 14. Flowchart of the optimal design stage.

Since the yield point of the S09 provided by the manufacturer is about 370 MPa, it has a safety factor above 1.3, even at a rotation speed higher than the required speed.

V. Optimal design for torque ripple reduction

Finally, an additional optimization is performed to improve some key performance variables of the design candidate from the previous stages, i.e., the initial and detailed design stages. In this optimal design process, it is important to utilize an optimization algorithm that has a small number of function evaluations because of the expensive computational cost based on FEA. In this research, we simply developed a surrogate model-based algorithm, which is intended to minimize the number of FEA evaluations.

To develop an effective surrogate model, Latin hypercube sampling (LHS) is used to achieve uniformly distributed samples; this is related to the quality of the interpolation function [42]-[43]. However, because the LHS is based on randomness, it does not always guarantee uniform sampling. Therefore, a space-filling (SF) method that directly performs sampling on the largest vacant space in the design domain is mixed and applied in this research.

Fig. 14 shows the flowchart of the proposed algorithm. Basically, sampling is performed based on LHS and SF in the sampling stage, but an adjustment strategy is applied to each iteration as follows. If the number of peaks is not improved in the continuous iteration, the sampling number by both LHS and SF is set to be reduced at the next iteration; this should reduce the function calls in the mostly converged condition. While, the number of peaks is updated, the sampling number at the next iteration is initialized. In this algorithm, the surrogate model is generated in each steps. Due to the relatively long analysis time with FEA for the objective function evaluations, it is not computational burden to iteratively develop the surrogate model.

To verify the developed optimization algorithm, it is tested by a mathematical test function as illustrated in Fig. 15. The test function has twenty-five local optima which can be represented by (19).

$$f(x_1,x_2) = 20 + x_1^2 - 10\cos 2\pi x_1 + x_2^2 - 10\cos 2\pi x_2 \quad (19)$$

This article has been accepted for publication in a future issue of this journal, but has not been fully edited. Content may change prior to final publication. Citation information: DOI 10.1109/ACCESS.2021.3105119, IEEE Access

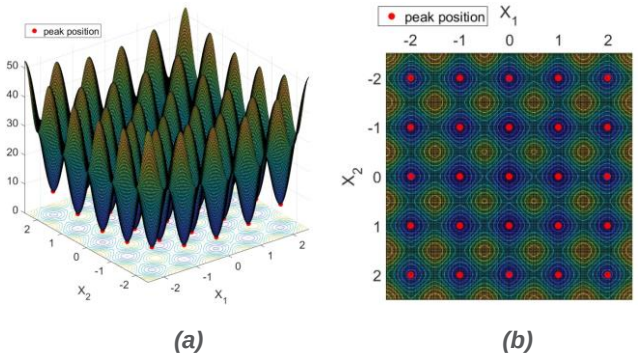

FIGURE 15. Illustration of the mathematical test function: (a) Mathematical test function (b) Peak positions.

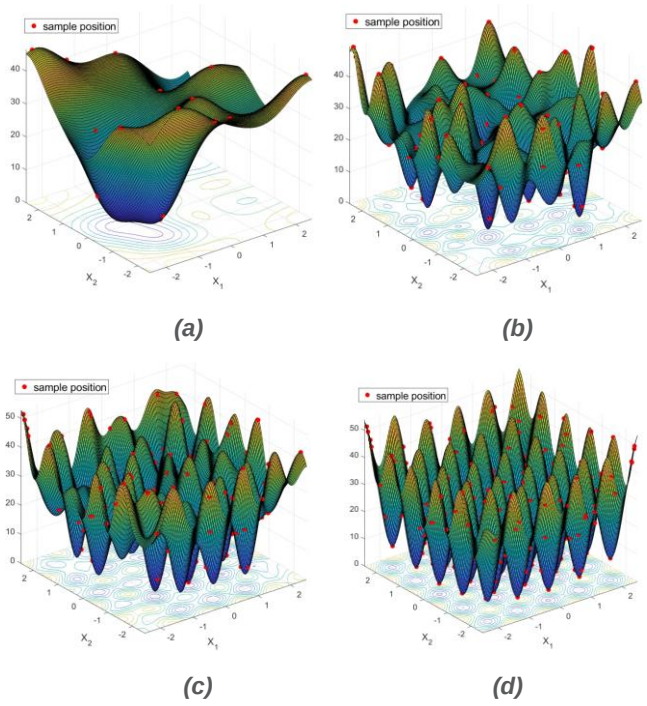

FIGURE 16. Illustration of the optimization process (a) Initial iteration (b) Iteration 4 (c) Iteration 7 (d) Iteration 12.

Then, the developed optimization algorithm was implemented to search the optima with ten initial samples. Here, the termination condition was set when the number of searched peaks is not improved in three consecutive iterations. Meanwhile, successful peak searches were judged when the interval of each coordinate with the actual optima positions was within 1 %. The surrogate models with the sample positions in initial, 4th, 7th, and final iterations in a test run are illustrated in Fig. 16. Compared to the BB-MOA, the average number of function evaluations was reduced from 329 to 220 with an identical convergence condition. Thus, the developed optimization algorithm can be expected more than 90 % time reduction compared to the commonly used probabilistic algorithms in multimodal design cases.

In this study, the torque ripple optimization of the IPMSM for the FCEV based on the reference model from the previous design stages is performed using the developed

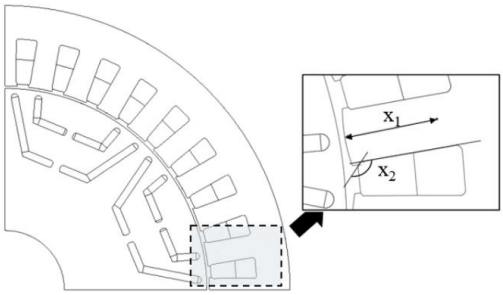

FIGURE 17. Design variables for the optimization.

TABLE II
OPTIMIZATION RESULTS OF CANDIDATES

Items	Candidate 1	Candidate 2	Candidate 3
x_1 [mm]	59.69	44.55	30.37
x_2 [°]	124.75	110.89	130.20
Cogging torque [Nm]	5.62 Nm	5.01 Nm	3.55 Nm
Average torque [Nm]	311.18 Nm	309.03 Nm	305.52 Nm
Torque ripple [%]	3.65%	3.34%	3.10%
Efficiency [%]	96.29%	96.26%	96.32%

algorithm. The torque ripple is the fluctuating torque resulting from the cogging torque and harmonic components of the back-EMF and driving current [44]-[46].

The torque fluctuation should be minimized because unwanted vibration and noise as well as loss of controllability can be caused. From the previous design results, the high-torque ripple is 5.87%, and an additional optimization process is required. As shown in Fig. 17, the arc radius (x_1) and shoe angle (x_2), which determine the topology of the stator tooth surface and the shoe, are utilized as the design variables, while the torque ripple is used as the objective function. The number of initial samples was set to 20 and the termination condition is when there is no improvement in the number of peaks. The optimization results provided some optimal candidates, as shown in Table II. Candidate 3 was chosen as the final optimum candidate due to its low cogging torque, low torque ripple, and high efficiency.

VI. Conclusion

This paper contributes to the SOD with an efficient, optimal design process for an IPMSM. The design is rapid and also accurate. The proposed strategy uses MEC, FEA, and an optimization algorithm by dividing the entire design process into initial, detailed, and optimal design stages. The proposed design strategy can be widely used as an effective design strategy for electric machines; various performance variables of a motor can be accurately considered and the computational cost can be remarkably reduced.

REFERENCES

[1] F. Un-Noor, S. Padmanaban, L. Mihet-Popa, M. N. Mollah, and F. A. Hossain, "Comprehensive study of key electric vehicle (EV) components, technologies, challenges, impacts, and future direction of development," *Energies*, vol 10, no. 8, pp.1217, Aug. 2017.

[2] K. Jyotheeswara Reddy and N. Sudhakar, "High voltage gain interleaved boost converter with neural network based MPPT controller for fuel cell based electric vehicle applications," *IEEE Access*, vol. 6, pp. 3899-3908, Jan. 2018.

[3] H. Bai, C. Liu, R. Ma, D. Paire and F. Gao, "Device-level modelling and FPGA-based real-time simulation of the power electronic system in fuel cell electric vehicle," *IET Power Electronics*, vol. 12, no. 13, pp. 3479-3487, Nov. 2019.

[4] K. Rahman, S. Jurkovic, P. J. Savagian, N. Patel and R. Dawsey, "Retrospective of electric machines for EV and HEV traction applications at general motors," *2016 IEEE Energy Conversion Congress and Exposition (ECCE)*, Milwaukee, WI, 2016, pp. 1-8.

[5] J.-C. Son, Y.-R. Kang, and D.-K. Lim, "Optimal design of IPMSM for FCEV using novel immune algorithm combined with steepest descent method," *Energies*, vol.13, no.13, pp. 3395, Jul. 2020.

[6] R. Thike and P. Pillay, "Mathematical model of an interior PMSM with aligned magnet and reluctance torques," *IEEE Trans. Transp. Electrif.*, vol. 6, no. 2, pp. 647-658, Jun. 2020.

[7] J. Liang, A. Parsapour, Z. Yang, C. Caicedo-Narvaez, M. Moallem and B. Fahimi, "Optimization of air-gap profile in interior permanent-magnet synchronous motors for torque ripple mitigation," *IEEE Trans. Transp. Electrif.*, vol. 5, no. 1, pp. 118-125, Mar. 2019.

[8] Takahashi and W. Hatsuse, "Novel criterion for reluctance torque utility of permanent magnet motors," *IEEE Trans. Energy Conversion*, vol. 34, no. 4, pp. 1751-1758, Dec. 2019.

[9] S. Wang, J. Kang, M. Degano, A. Galassini and C. Gerada, "An accurate wide-speed range control method of IPMSM considering resistive voltage drop and magnetic saturation," *IEEE Trans. Ind. Electron.*, vol. 67, no. 4, pp. 2630-2641, Apr. 2020.

[10] G. Dajaku and D. Gerling, "Stator slotting effect on the magnetic field distribution of salient pole synchronous permanent-magnet machines," *IEEE Trans. Magn.*, vol. 46, no. 9, pp. 3676-3683, Sep. 2010.

[11] L. Zhu, S. Z. Jiang, Z. Q. Zhu and C. C. Chan, "Analytical modeling of open-circuit air-gap field distributions in multisegment and multilayer interior permanent-magnet machines," *IEEE Trans. Magn.*, vol. 45, no. 8, pp. 3121-3130, Aug. 2009.

[12] S. Han, T. M. Jahns and W. L. Soong, "A magnetic circuit model for an IPM synchronous machine incorporating moving airgap and cross-coupled saturation effects," *2007 IEEE International Electric Machines & Drives Conference*, Antalya, 2007, pp. 21-26.

[13] R. Qu and T. A. Lipo, "Analysis and modeling of air-gap and zigzag leakage fluxes in a surface-mounted permanent-magnet Machine," *IEEE Trans. Ind. Applicat.*, vol. 40, no. 1, pp. 121-127, Jan./Feb. 2004.

[14] H. -K. Yeo, D. -K. Lim, D. -K. Woo, J. -S. Ro and H. -K. Jung, "Magnetic equivalent circuit model considering overhang structure of a surface-mounted permanent-magnet Motor," *IEEE Trans. Magn.*, vol. 51, no. 3, pp. 1-4, Mar. 2015, Art. no. 8201004.

[15] Y. Kano, T. Kosaka and N. Matsui, "Simple nonlinear magnetic analysis for permanent-magnet motors," *IEEE Trans. Ind. Applicat.*, vol. 41, no. 5, pp. 1205-1214, Sep./Oct. 2005.

[16] M. Hsieh and Y. Hsu, "A generalized magnetic circuit modeling approach for design of surface permanent-magnet machines," *IEEE Trans. Ind. Electron.*, vol. 59, no. 2, pp. 779-792, Feb. 2012.

[17] P. Liang, F. Chai, Y. Yu and L. Chen, "Analytical model of a spoke-type permanent magnet synchronous in-wheel motor with trapezoid magnet accounting for tooth saturation," *IEEE Trans. Ind. Electron.*, vol. 66, no. 2, pp. 1162-1171, Feb. 2019.

[18] M. R. Mohammad, K. Kim and J. Hur, "Design and analysis of a spoke type motor with segmented pushing permanent magnet for concentrating air-gap flux density," *IEEE Trans. Magn.*, vol. 49, no. 5, pp. 2397-2400, May 2013.

[19] J. P. Wang, D. K. Lieu, W. L. Lorimer and A. Hartman, "Comparison of lumped parameter and finite element magnetic modeling in a brushless DC motor," *IEEE Trans. Magn.*, vol. 33, no. 5, pp. 4092-4094, Sep. 1997.

[20] J. -K. Kim, S. -W. Joo, S. -C. Hahn, J. -P. Hong, D. -H. Kang, and D. -H. Koo, "Static characteristics of linear BLDC motor using equivalent magnetic circuit and finite element method," *IEEE Trans. Magn.*, vol. 40, no. 2, pp. 742-745, Mar. 2004.

[21] E. C. Lovelace, T. M. Jahns and J. H. Lang, "A saturating lumped-parameter model for an interior PM synchronous machine," *IEEE Trans. Ind. Applicat.*, vol. 38, no. 3, pp. 645-650, May/Jun. 2002.

[22] P. Akiki, M. Hassan, J. Vannier, M. Bensetti, D. Prieto, B. Daguse, and M. McCelland, "Nonlinear analytical model for a multi-V-shape IPM with concentrated winding," *IEEE Trans. Ind. Applicat.*, vol. 54, no. 3, pp. 2165-2174, May/Jun. 2018.

[23] D. -K. Lim, K. -P. Yi, D. -K. Woo, H. -K. Yeo, J. -S. Ro, C. -G. Lee, and H. -K. Jung, "Analysis and design of a multi-Layered and multi-segmented interior permanent magnet motor by using an analytic method," *IEEE Trans. Magn.*, vol. 50, no. 6, pp. 1-8, Jun. 2014, Art. no. 8201308.

[24] J. -G. Lee, D. -K. Lim and H. -K. Jung, "Analysis and design of interior permanent magnet synchronous motor using a sequential-stage magnetic equivalent circuit," *IEEE Trans. Magn.*, vol. 55, no. 10, pp. 1-4, Oct. 2019, Art. no. 7501004.

[25] M. Amrhein and P. T. Krein, "Induction machine modeling approach based on 3-D magnetic equivalent circuit framework," *IEEE Trans. Energy Conversion*, vol. 25, no. 2, pp. 339-347, Jun. 2010.

[26] S. D. Sudhoff, B. T. Kuhn, K. A. Corzine and B. T. Branecky, "Magnetic equivalent circuit modeling of induction motors," *IEEE Trans. Energy Conversion*, vol. 22, no. 2, pp. 259-270, Jun. 2007.

[27] C. –H. Yoo, D. –K. Lim, and H. –K. Jung, "A novel multimodal optimization algorithm for the design of electromagnetic machines," *IEEE Trans. Magn.*, vol. 51, no. 3, Mar. 2016, Art. no. 8201304.

[28] M.-H. Hwang, J. –H. Han, D. –H. Kim, and H. –R. Cha, "Design and analysis of rotor shapes for IPM motors in EV power traction platforms," *Energies*, vol. 11, no. 10, pp. 2601, Sep. 2018.

[29] Y. Yang, S. Castano, R. Yang, M. Kasprzak, B. Bilgin, A. Sathyan, H. Dadkhah, and A. Emadi, "Design and comparison of interior permanent magnet motor topologies for traction applications," *IEEE Trans. Transp. Electrif.*, vol. 3, no. 1, pp. 86-97, Mar. 2017.

[30] Wang, Y. Jia and W. L. Soong, "Comparison of five topologies for an interior permanent-magnet machine for a hybrid electric vehicle," *IEEE Trans. Magn.*, vol. 47, no. 10, pp. 3606-3609, Oct. 2011.

[31] J-. M. Mun, G-. J. Park, S-. H. Seo, D-. W. Kim, Y-. J. Kim and S-. Y. Jung, "Design characteristics of IPMSM with wide constant power speed range for EV traction," *IEEE Trans. Magn.*, vol. 53, no. 6, pp. 1-4, Jun. 2017, Art. no. 8105104.

[32] D. Zarko, D. Ban and T. A. Lipo, "Analytical solution for cogging torque in surface permanent-magnet motors using conformal mapping," *IEEE Trans. Magn.*, vol. 44, no. 1, pp. 52-65, Jan. 2008.

[33] D. Zarko, D. Ban and T. A. Lipo, "Analytical calculation of magnetic field distribution in the slotted air gap of a surface permanent-magnet motor using complex relative air-gap permeance," *IEEE Trans. Magn.*, vol. 42, no. 7, pp. 1828-1837, Jul. 2006.

[34] H. Gurleyen and E. Mese, "A Nonlinear q-Axis Inductance Modeling of a 12-Slot 10-Pole IPM using approximate analytical methods," *IEEE Trans. Energy Conversion*, vol. 35, no. 2, pp. 621-630, Jun. 2020.

[35] S. Wu, L. Guo, H. Wang, Y. Cao, T. Shi and C. Xia, "Inductance calculation of interior permanent magnet machines considering asymmetrical saturation of the bridge," *IEEE Trans. Magn.*, vol. 55, no. 11, pp. 1-11, Nov. 2019, Art. no. 8107511.

[36] X. Zhu, W. Wu, S. Yang, Z. Xiang and L. Quan, "Comparative design and analysis of new type of flux-intensifying interior permanent magnet motors with different q-Axis rotor flux barriers," *IEEE Trans. Energy Conversion*, vol. 33, no. 4, pp. 2260-2269, Dec. 2018.

[37] C. Jungreuthmayer, T. Bauml, O. Winter, M. Ganchev, H. Kapeller, A. Haumer, and C. Kral, "A detailed heat and fluid flow analysis of an internal permanent magnet synchronous machine by means of computational fluid dynamics," *IEEE Trans. Ind. Electron.*, vol. 59, no. 12, pp. 4568-4578, Dec. 2012.

[38] G. Du, W. Xu, J. Zhu and N. Huang, "Power loss and thermal analysis for high-power high-speed permanent magnet machines," *IEEE Trans. Ind. Electron.*, vol. 67, no. 4, pp. 2722-2733, Apr. 2020.

[39] Y. Gai, M. Kimiabeigi, Y. Chong, J. Widmer, X. Deng, M. Popescu, J. Goss, D. Staton, and A. Steven "Cooling of automotive traction motors: Schemes, examples, and computation methods," *IEEE Trans. Ind. Electron.*, vol. 66, no. 3, pp. 1681-1692, Mar. 2019.

[40] V. Madonna, A. Walker, P. Giangrande, G. Serra, C. Gerada and M. Galea, "Improved thermal management and analysis for stator end-windings of electrical machines," *IEEE Trans. Ind. Electron.*, vol. 66, no. 7, pp. 5057-5069, Jul. 2019.
[41] R. Burke, A. Giedymin, Z. Wu, H. Chuan, N. Bourne and J. G. Hawley, "A lumped parameter thermal model for single-sided AFPM machines with experimental validation," *IEEE Trans. Transp. Electrif.*, vol. 6, no. 3, pp. 1065-1083, Sep. 2020.
[42] K. Crombecq, E. Laermans, and T. Dhaene, "Efficient space-filling and non-collapsing sequential design strategies for simulation-based modeling," *European Journal of Operational Research*, vol. 214, no. 3, pp. 683-696, Nov. 2011.
[43] F. Viana, G. Venter, and V. Balabanov, "An algorithm for fast optimal Latin hypercube design of experiments," *Int. J. Numer. Meth. Engng.*, vol. 82, no. 2, pp. 135-156. Apr. 2010.
[44] W. Deng and S. Zuo, "Electromagnetic Vibration and Noise of the Permanent-Magnet Synchronous Motors for Electric Vehicles: An Overview," *IEEE Trans. Transp. Electrif.*, vol. 5, no. 1, pp. 59-70, Mar. 2019.
[45] H. Mahmoudi, M. Aleenejad and R. Ahmadi, "Torque Ripple Minimization for a Permanent Magnet Synchronous Motor Using a Modified Quasi-Z-Source Inverter," *IEEE Trans. Power Electron.*, vol. 34, no. 4, pp. 3819-3830, Apr. 2019.
[46] Z. Zeng, C. Zhu, X. Jin, W. Shi and R. Zhao, "Hybrid Space Vector Modulation Strategy for Torque Ripple Minimization in Three-Phase Four-Switch Inverter-Fed PMSM Drives," *IEEE Trans. Ind. Electron.*, vol. 64, no. 3, pp. 2122-2134, Mar. 2017.

Jae-Gil Lee was born in Busan, South Korea, in 1987. He received a B.S. in electrical engineering from Pusan National University, Busan, South Korea, in 2013, and a Ph.D. in electrical engineering from Seoul National University, Seoul, through the combined master's and Ph.D. program in 2020. He is currently a postdoctoral researcher with the Korea Electronics Technology Institute, South Korea. His research interests include analysis and optimal design of electrical machines.

Dong-Kuk Lim (Member, IEEE) was born in Seoul, South Korea, in 1984. He received a B.S. in electrical engineering from Dongguk University, Seoul, South Korea, in 2010, and a Ph.D. in electrical engineering from Seoul National University, Seoul, through the combined master's and Ph.D. program in 2017.
In 2017, he was with the Electrical Power Engineering Team, Hyundai Mobis Company, South Korea, as a Senior Research Engineer. He is currently an Assistant Professor with the School of Electrical Engineering, University of Ulsan, South Korea. His research interests include analysis and optimal design of electrical machines.